## Research Highlights

A novel, more robust algorithm with improved accuracy in peak extraction especially for asymmetrical response signals in confocal microscopy is given and validated. Improved accuracy is demonstrated for height and layer thickness measurements.

**Abbreviations:** NA, numerical aperture; LC, linear centroid; SC, square centroid; PF, parabolic fitting; GF, Gaussian fitting; CF, cubic fitting; SNR, signal-to-noise ratio; Cr, chromium.

ORIGINAL ARTICLE

Field of the paper

# A novel cubic-exp evaluation algorithm considering non-symmetrical axial response signals of confocal microscopes

**Sebastian Hagemeier[1] | Tobias Pahl[1] | Johannes Breidenbach[1] | Peter Lehmann[1]**

The depth discrimination in confocal microscopy is based on the digital analysis of depth response signals obtained by each camera pixel during measurement. Various signal processing algorithms are used for this purpose. The accuracy of these algorithms is inter alia restricted by the axial symmetry of the signals. However, in practice response signals are rather asymmetrical especially in case of measurement objects with critical surface structures such as edges or steep flanks. We present a novel signal processing algorithm based on an exponential function with a cubic argument to handle asymmetrical and also symmetrical depth response signals. Results obtained by this algorithm are compared to those of commonly used signal processing algorithms. It turns out that the novel algorithm is more robust, more accurate and exhibits a repeatability of a similar order compared to other algorithms.

**Keywords** — Confocal microscope, *signal analysis*, cubic-exp algorithm, asymmetrical signal, evaluation algorithm, layer thickness, aberration

[1]Measurement Technology, Department of Electrical Engineering and Computer Science, University of Kassel, Wilhelmshöher Allee 71, 34121 Kassel, Germany

**Correspondence**
Sebastian Hagemeier, Measurement Technology, Electrical Engineering and Computer Science, Kassel, Hessen, 34121, Germany
Email: sebastian.hagemeier@uni-kassel.de

**Funding information**

## Introduction

Confocal microscopy is a widely used optical measuring method for surface topography measurement with texture heights in the range of micro- and nanometers. Due to its increased lateral resolution compared to other optical mea-

surement methods as well as its property to fade out the light out of focus of the microscope objective, a confocal microscope is an attractive instrument for a variety of applications in industry and science. In order to discriminate height values from the measured intensity data, several signal evaluation algorithms, such as the linear centroid approach (Ruprecht et al., 2002) as well as nonlinear fitting algorithms e.g. parabolic, Gaussian, and $\text{sinc}^2$ (Tan et al., 2015) algorithms, are frequently used. The performances of these approaches are compared in several studies (Rahlves et al., 2017; Liu et al., 2017; Shao et al., 2018). They typically expect axial response signals, which are symmetrical with respect to the focus point. However, spherical aberrations (Wilson and Carlini, 1989; Rahlves et al., 2015) and other influences depending on the surface to be measured result in non-symmetric response signals. This leads to systematic deviations in height discrimination by using the approaches mentioned above.

In this work, we present a novel fitting algorithm, which is based on an exponential function with a cubic argument to handle non-symmetrical signals more accurately compared to established signal processing algorithms. The new algorithm is validated using depth responses obtained from rectangular grating structures and a tilted plane mirror. For this purpose, simulated signals are used for validation in order to avoid effects resulting from signal noise and real surface deviations. Furthermore, repeatabilities obtained from the novel algorithm are compared with those of centroid, parabolic and Gaussian fitting algorithms. It is investigated how well the different signal processing approaches can handle consecutive response signals of varying axial sample point locations. Finally, the algorithms are compared by use of response signals obtained from a layer thickness standard using a commercial confocal microscope. The analysis shows that the cubic fitting algorithm locates the position of the detected response maximum most reliably. An improvement in the detection of the signal maximum using a fitting function of increased order is already mentioned by Kim et al. (Kim et al., 2006). Chen et al. (Chen et al., 2019) present a corrected parabolic fitting algorithm to reduce systematic deviations of a parabolic fitting. This algorithm is applied to symmetrical and asymmetrical spectra of a chromatic confocal microscope. It is shown that the results of the corrected parabolic fitting algorithm exhibit a lower standard deviation compared to other algorithms. However, an improvement for detecting the maximum of non-symmetrical signals is not shown. Another approach is given by Seewig et al. (Seewig et al., 2013) where a robust signal processing of noisy response signals is performed using Maximum-Likelihood estimation. An asymmetrical shape of the intensity signal is significantly suppressed during the signal processing. However, the focus is on suppressing signal noise and an analysis of asymmetrical compared to symmetrical depth response signals is not discussed. Furthermore, signal filtering can lead to a loss of information.

## 1 | AXIAL RESPONSE SIGNAL FORMATION AND EVALUATION ALGORITHM

First, the formation of an axial response signal of a confocal microscope is briefly discussed in this section. Then, the cubic signal processing algorithm as well as further approaches such as centroid, parabolic and Gaussian fitting algorithms are introduced for comparison.

### 1.1 | Signal formation

The working principle of a confocal microscope is based on microscopic imaging. While the temporal coherence of the illumination source does not affect the basic principle of confocal microscopy, spatially coherent illumination is crucial. Spatial coherence can be achieved due to a pinhole located in the illumination arm of the microscope as schematically illustrated in Fig. 1. Due to the microscope objective lens an image of the pinhole occurs on the specimen's surface. Light scattered from the specimen is collected by the objective lens and focused to the detector pinhole. If the axial

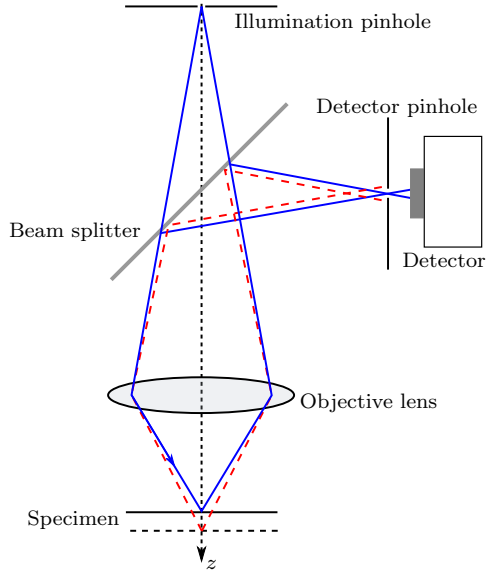


**FIGURE 1** Schematic illustration of a confocal microscope. The blue line illustrates the imaging beam path, if the specimen is in focus of the microscope objective. An out of focus beam path is exemplarily represented by the red dashed line.

location of the surface under investigation matches the working distance of the microscope objective (visualized by the blue line), the collected light passes the detector pinhole. In this case the maximum intensity is detected by the detector or the corresponding camera pixel. On the other hand, the detected intensity decreases with increasing or decreasing distance of the surface under investigation with respect to the axial focus position. Consequently, if the distance between objective lens and specimen is continuously changed during the depth scan, a depth response signal results. Compared to conventional optical microscopes the depth response signal of a confocal microscope is characterized by a narrow intensity peak, which falls to zero if the surface is far away from the focus position. A more detailed description of the depth response signal is given in (Corle and Kino, 1996; Pahl et al., 2021). Signals measured by a confocal microscope are exemplarily depicted in Fig. 2. These signals are obtained from a rectangular surface structure of 6 µm period length using the commercial confocal microscope µsurf custom (Nanofocus AG) with a numerical aperture (NA) of 0.95 using a cyan LED for illumination (Hagemeier et al., 2019; Hagemeier, 2022). For better comparability the intensity curves are normalized and the locations of the maximum are axially shifted to zero. The signal depicted in Fig. 2a is obtained from an upper plateau of the rectangular structure and nearly symmetrical, whereas the signal presented in Fig. 2b is obtained from an edge of 190 nm height of the structure and shows some asymmetry. Consequently, both symmetrical and asymmetrical signals occur from the rectangular grating enabling to validate signal processing algorithms for both, asymmetrical and symmetrical response signals.

## 1.2 | Signal analysis

In order to discriminate height information from confocal response signals several signal processing algorithms are used in practice. One of the fastest and most frequently used computation algorithm is the centroid algorithm, repre-

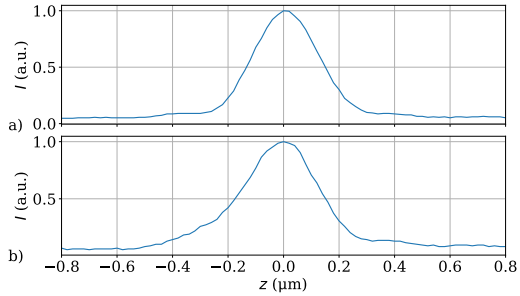


**FIGURE 2** Normalized depth response signals measured by a confocal microscope with an NA of 0.95 at a) the upper plateau and b) the edge of a rectangular surface structure.

sented by

$$h_{\mathrm{c,lin}} = \frac{\sum_{j=0}^{N-1} z(j) I(j)}{\sum_{j=0}^{N-1} I(j)} \tag{1}$$

for linear or

$$h_{\mathrm{c,sq}} = \frac{\sum_{j=0}^{N-1} z(j) I^2(j)}{\sum_{j=0}^{N-1} I^2(j)}. \tag{2}$$

for square relation, where the intensity of the response signal is represented by $I(j)$ at the position $z(j)$ of the depth scan in $z$ direction. Further approaches rely on least squares approximation of the measured intensity signal by a known mathematical function such as a parabola or a Gaussian function. A polynomial function of order $n$ can be described by

$$f(z) = a_{\mathrm{n}} z^n + \cdots + a_1 z + a_0, \qquad z \in \{z_l, \ldots, z_r\}, \tag{3}$$

where the indices $l$ and $r$ represent the left and right border of the intensity tuple above a certain threshold. The parameters $a_i$ ($i \in 1, \ldots, n$) are determined by solving the equation system

$$\begin{bmatrix} I(z_l) \\ \vdots \\ I(z_r) \end{bmatrix} = \begin{bmatrix} z_l^n & \cdots & z_l & 1 \\ \vdots & \vdots & \vdots & \vdots \\ z_r^n & \cdots & z_r & 1 \end{bmatrix} \begin{bmatrix} a_{\mathrm{n}} \\ \vdots \\ a_1 \\ a_0 \end{bmatrix} \tag{4}$$

using QR decomposition. In case of a parabola ($n$=2) the axial position of the maximum results from

$$h_{\mathrm{square}} = -\frac{a_1}{2a_2}. \tag{5}$$

The same procedure can be used to calculate the axial position of the maximum of a fitted Gaussian function. Here, the natural logarithm of the intensity $I(z)$ is taken in order to receive the argument of the exponential function, leading to

$$\begin{bmatrix} \ln\left(I(z_l)\right) \\ \vdots \\ \ln\left(I(z_r)\right) \end{bmatrix} = \begin{bmatrix} z_l^2 & z_l & 1 \\ \vdots & \vdots & \vdots \\ z_r^2 & z_r & 1 \end{bmatrix} \begin{bmatrix} a_2 \\ a_1 \\ a_0 \end{bmatrix}. \tag{6}$$

These signal processing algorithms are suitable for symmetrical depth response signals. However, as shown above measured depth response signals are often asymmetric, where the strength of asymmetry depends on the surface texture and the components of the confocal microscope. Even the depth response signal in Fig. 2a obtained from a flat surface section is not perfectly symmetric.

Asymmetries can be considered by use of an exponential function with a cubic argument ($n$=3) for fitting confocal signals. The fitting procedure is similar to that of the Gaussian according to Eq. (6) and the axial position of the maximum can be taken from

$$z_{1,2} = -\frac{a_2}{3a_3} \pm \sqrt{\left(\frac{a_2}{3a_3}\right)^2 - \frac{a_1}{3a_3}}. \tag{7}$$

Since a cubic function comprises two extreme values (a maximum and a minimum) and only the maximum is relevant, the correct axial position arises from

$$h_{\text{cubic}} = \begin{cases} z_1, & I(z_1) > I(z_2) \\ z_2, & \text{otherwise.} \end{cases} \tag{8}$$

Note that the presented evaluation algorithm determines the axial position of a single depth response curve and must be applied to each signal, i.e. each camera pixel in a full-field measuring confocal microscope.

## 2 | VALIDATION OF DEPTH DISCRIMINATION ALGORITHMS

In order to validate the different evaluation algorithms, simulated depth response signals obtained from certain surface textures are investigated using a rigorous simulation model (Pahl et al., 2021). As the simulated signals show a good correspondence to measured depth response signals, they are suitable for validation of the previously introduced depth discrimination algorithms. Further, the use of the simulation software instead of a real confocal microscope enables to suppress or to investigate certain influences. If not explicitly added, simulated depth response signals are for example not superimposed by noise and hence the influence of noise can be studied separately superposing simulated signals with artificial noise of different SNR values. Another benefit of simulated response signals is due to the knowledge of the texture of the surface under investigation.

In this work, the depth response signals are simulated for a confocal microscope with an NA of 0.95. As a light source a cyan LED with a central wavelength of 505 nm and a typical spectral distribution is considered. If not other specified, the step size $\Delta z$ of the depth scan is 20 nm. For signal processing, the previously introduced algorithms, linear centroid (LC), square centroid (SC), parabolic fitting (PF), Gaussian fitting (GF) and exponential function with cubic argument in the following denoted by cubic fitting (CF), are used and compared. Except for Sec. 2.3, no filtering

is applied to the obtained depth response signals.

## 2.1 | Rectangular grating

First rectangular gratings of the RS-N standard from Simetrics (SiMETRICS GmbH, 2009) are assumed. The longest period of 6 µm and a step height of 190 nm are used to calculate depth response signals, resulting in the profiles depicted in Fig. 3. Before applying the depth discrimination algorithm a section of the signal is chosen for further evaluation using a threshold with respect to the maximum intensity of the investigated signal. Different threshold values are used for the height profiles depicted in Fig. 3. Figure 3a, b, and c show five profiles, which result from threshold values of 0.5, 0.7, and 0.9, respectively. These profiles exhibit slightly different curve shapes. While the profiles calculated by the CF algorithm (red curve) for different thresholds are nearly identical, those determined by the other algorithms vary as it becomes obvious by comparison of Figs. 3a, b and c. This is especially observable at the edges of the profiles, where asymmetrical response signals occur. The profiles determined with the LC (orange) and SC (purple) algorithms show a similar course.

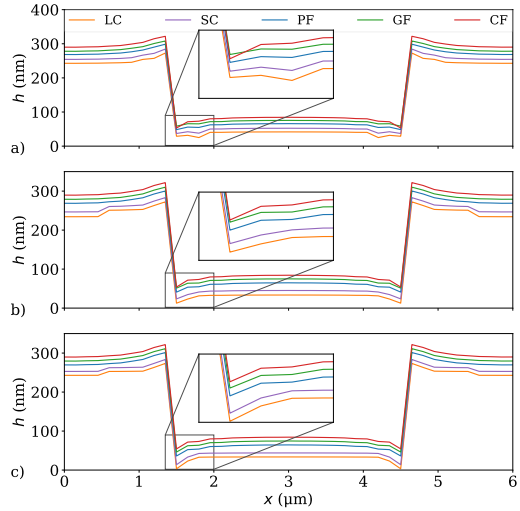


**FIGURE 3** Simulated results from a rectangular surface structure with a period length of 6 µm and a nominal step height of 190 nm. The height values are obtained using linear centroid (LC), square centroid (SC), parabolic fitting (PF), Gaussian fitting (GF) and cubic fitting (CF) for the threshold factors: a) 0.5, b) 0.7 and c) 0.9.

Whereas the response signals obtained from the upper and lower plateau are nearly symmetric (compare Fig. 2a), the response signals obtained at the edges of the grating reveal an asymmetric shape. This is probably a consequence of the so-called batwing effect (Xie, 2017), which occurs through interference of light diffracted at the edges of the investigated surface structure and leads to the overshoots shown in Fig. 3. Such an asymmetric depth response signal obtained at the lateral position $x = 1.5$ µm is depicted in Fig. 4 and used to demonstrate how well the different approaches fit the signal. Figure 4 shows the intensity signal (blue), the different fitting curves for threshold factors of 0.5, 0.7, and 0.9 and the calculated axial positions of the intensity maximum represented by crosses of different colors. The fitting curves of the parabolic (purple) and the Gaussian (green) algorithms deviate strongly, whereas those

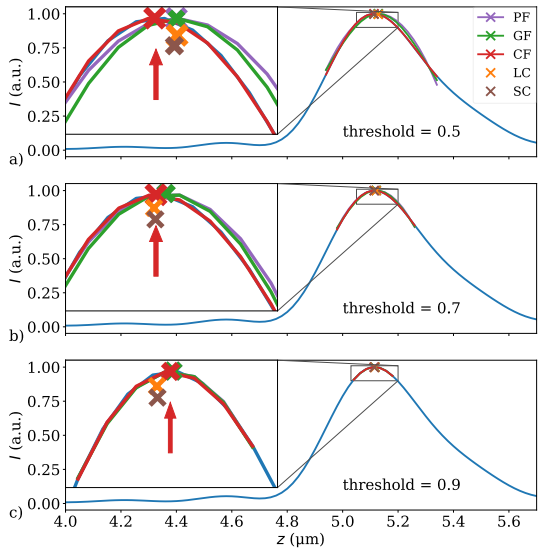


**FIGURE 4** Normalized response signals (blue) obtained from the rectangular structure shown in Fig. 3 at the lateral position x = 1.5 µm. The axial positions of the correct maximum (see arrow) and the maximum determined by several signal processing algorithms are marked by different colors.

of the cubic approach (red) fit the intensity signal quite well. Consequently, the axial positions determined by PF and GF approaches differ significantly from the correct position. Similar deviations are obtained for the LC (orange) and SC (brown) methods as a consequence of the asymmetry. Due to the superior performance of the CF approach, the determined axial position of this method shows the smallest deviation from the depth response signal. In the case of a threshold of 0.7, the deviation between the fitting curves generated by PF and GF approaches reduces compared to the results obtained for the threshold of 0.5 and thus also the deviation between the determined axial positions, representing the estimated height values decrease. The axial positions determined by the LC and SC methods are significantly closer to the intensity maximum as well. Hence, with an increased threshold value an improved determination of the height value seems to be achieved. However, in the case of a threshold of 0.9, the axial position determined by LC and SC deviates stronger compared to the values determined for a threshold of 0.7. This increased deviation results from an unequal number of sampling points around the maximum of the intensity signal, which affects the height values determined by PF and GF less. However, a higher threshold value has the consequence that the number of sampling points used for signal processing decreases and thus a higher measurement uncertainty is to be expected in the presence of noise. Note that in all cases the CF method fits the corresponding response signal well and thus, the determined height values are constant. Therefore, the overshoots caused by the batwing effect are best approximated using the CF approach.

In order to visualize the quality of the different fitting algorithms in numbers, the standard deviations of the fitted curves obtained by the different algorithms with respect to the measured intensity signal are listed in Tab. 1. For a threshold of 0.5, the fitting curves calculated using the PF and GF approaches show much higher deviations compared to the CF approach, as expected from Fig. 4. Only above a threshold value of 0.9 do the deviations of the PF and GF approaches reach a value comparable to that of the CF approach at a threshold value of 0.5. For all investigated thresholds, the CF approach shows the lowest standard deviations, followed by the GF and finally, the PF approaches.

| Threshold | $\sigma_{PF}$ (‰) | $\sigma_{GF}$ (‰) | $\sigma_{CF}$ (‰) |
|---|---|---|---|
| 0.5 | 27.278 | 20.045 | 1.208 |
| 0.6 | 16.315 | 12.804 | 0.669 |
| 0.7 | 8.310 | 7.433 | 0.287 |
| 0.8 | 3.381 | 2.956 | 0.085 |
| 0.9 | 0.923 | 1.080 | 0.015 |

**TABLE 1** Standard deviations of the fitted curves obtained from the different signal processing algorithms (shown in Fig. 4) with respect to the measured intensity signal.

Although the response signals obtained from the upper and lower plateaus are nearly symmetric, depending on the signal processing algorithm the resulting profiles shown in Fig. 3 differ. In order to compare the measured step heights, the height differences $\Delta h$ between height values at the lateral positions $x$ = 3 µm and 6 µm are summarized in Tab. 2. Comparison between the height differences shows a variation depending on the applied threshold value. Height differences obtained from the profiles determined by the centroid algorithms exhibit the highest variation (see $\sigma_{\Delta h}$), followed by those of the PF and GF algorithms. On the other hand, the height differences of the profiles calculated by the CF method are nearly constant. Here, the reason is the same as for the asymmetrical signals discussed before. The CF approach fits the depth response signals best and thus the variation is low. However, all determined height differences are higher than the nominal step height of 190 nm. For comparison, a profile of the rectangular

| Threshold | 0.5 | 0.6 | 0.7 | 0.8 | 0.9 | $\sigma_{\Delta h}$ |
|---|---|---|---|---|---|---|
| $\Delta h_{LC}$ (nm) | 201.1 | 208.4 | 200.8 | 200.6 | 209.3 | 3.94 |
| $\Delta h_{SC}$ (nm) | 201.9 | 207.4 | 201.5 | 201.1 | 209.0 | 3.3 |
| $\Delta h_{PF}$ (nm) | 202.7 | 204.0 | 204.0 | 204.6 | 205.2 | 0.83 |
| $\Delta h_{GF}$ (nm) | 202.7 | 203.4 | 204.2 | 204.8 | 205.1 | 0.89 |
| $\Delta h_{CF}$ (nm) | 205.6 | 205.9 | 205.6 | 205.6 | 205.6 | 0.12 |

**TABLE 2** Height differences $\Delta h$ of the rectangular profiles shown in Fig. 3. $\sigma_{\Delta h}$ represents the empirical standard deviation determined for height differences of each signal processing algorithm.

grating is measured by the commercial confocal microscope characterized by the same parameters (NA = 0.95 and cyan LED light source with a center wavelength of 505 nm). Similar to the results listed in Tab. 2 the step heights (approx. 201 nm) of the measured grating are higher compared to the nominal value, as shown in Fig. 5. In order to analyze the overestimation of simulated and measured grating heights, simulations are performed for gratings of same height (190 nm) but with different period lengths $L$. Figure 6 displays simulated grating profiles obtained by GF algorithm for $L$ = 3 µm, $L$ = 6 µm and $L$ = 10 µm. It should be mentioned that a monochromatic light source is assumed in the simulation, since simulations considering broader spectral bandwidths are time consuming and the results shown here are sufficient to explain the overestimation. Hence, the result obtained for $L$ = 6 µm in Fig. 6 slightly differs from the profiles presented in Fig. 3.

Comparing the grating profiles in Fig. 6, the grating with $L$ = 3 µm shows the highest height difference, whereas the

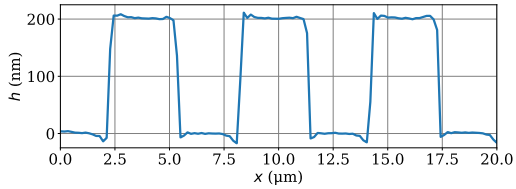


**FIGURE 5** Measured rectangular grating with 6 µm period length obtained from the RS-N standard using a commercial 100x confocal microscope with an NA of 0.95.

height difference for $L = 10\,\mu m$ almost corresponds to the nominal height. Therefore, the overestimation of measured step heights can be explained by the overshoots, which slightly decay with distance to the edges. If the period length of the grating is too small, neighboring edges influence each other due to diffraction and the measured height differences exceed the nominal height values leading to the obtained overestimation.

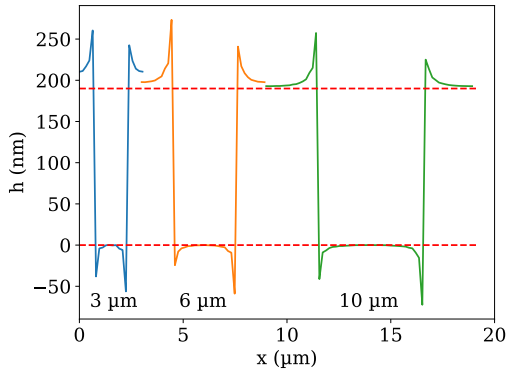


**FIGURE 6** Simulated rectangular profiles of period lengths (3 µm, 6 µm and 10 µm) obtained by use of the Gaussian fit (GF) algorithm. The red dashed lines represent the upper and lower levels corresponding to the nominal height of 190 nm.

A further example of interest is given a rectangular grating with a period length of 400 nm and a step height of 140 nm, taken from the same RS-N standard. Simulated profiles resulting from the different signal processing algorithms are depicted in Fig. 7 for several thresholds. As expected, the resulting profiles do not correspond to the nominal rectangular grating profile, since the period length of the grating is close to the lateral optical resolution limit of the confocal microscope considered by the simulation program. While the profiles calculated by the fitting algorithms are sinusoids, the profiles determined by the centroid algorithms exhibit a stepped shape. Due to the fact that the surface's period length is close to the lateral resolution limit, only scattered light up to the first diffraction order is captured by the microscope objective lens and thus, a sinusoidal shape is expected. Hence, the results obtained by the fitting methods appear to be more correct compared to those obtained by the centroid algorithms. A comparison

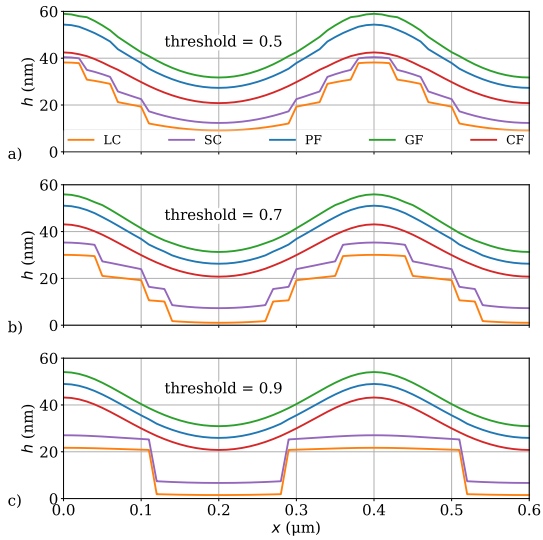


**FIGURE 7** Simulated profiles of a rectangular grating with a period length of 400 nm and a step height of 140 nm. The confocal depth response signals are simulated and evaluated using linear centroid (LC), square centroid (SC), parabolic fitting (PF), Gaussian fitting (GF) and cubic fitting (CF).

between the profiles depicted in the Figs. 7a, b and c shows that the profiles calculated by the CF method (red) are again nearly equal in amplitude. The peak-to-valley amplitudes $\Delta h$ according to Tab. 3 are calculated from the height values at the lateral positions $x$ = 0.2 µm and 0.4 µm. While the height differences $\Delta h_{CF}$ are nearly constant, the

| Threshold | 0.5 | 0.6 | 0.7 | 0.8 | 0.9 | $\sigma_{\Delta h}$ |
|---|---|---|---|---|---|---|
| $\Delta h_{LC}$ (nm) | 29.1 | 36.7 | 29.0 | 20.4 | 20.2 | 6.20 |
| $\Delta h_{SC}$ (nm) | 28.1 | 33.9 | 28.0 | 20.8 | 20.4 | 5.08 |
| $\Delta h_{PF}$ (nm) | 27.0 | 26.7 | 24.8 | 23.8 | 23.1 | 1.55 |
| $\Delta h_{GF}$ (nm) | 27.2 | 26.0 | 24.6 | 24.0 | 23.1 | 1.46 |
| $\Delta h_{CF}$ (nm) | 21.7 | 22.0 | 22.3 | 22.3 | 22.4 | 0.26 |

**TABLE 3** Measured height differences $\Delta h$ of the simulated rectangular profiles shown in Fig. 7. $\sigma_{\Delta h}$ represents the empirical standard deviation determined for height differences of each signal processing algorithm.

determined height values of the other signal processing algorithms exhibit higher standard deviations $\sigma_{\Delta h}$. The calculated height values $\Delta h_{LC}$ show the strongest variation, followed by $\Delta h_{SC}$. In contrast, the height values obtained by the fitting methods show lower variations. All determined height differences are significantly lower than the nominal step height of 140 nm. This is a consequence of the optical resolution limit, which with regard to the period length of the rectangular grating leads to a considerable low-pass filtering effect of the measured profile. These results are in good agreement to profiles measured by a commercial confocal microscope with an NA of 0.95 as presented by Pahl et al. (Pahl et al., 2021).

## 2.2 | Tilted plane mirror

This section is intended to investigate how well the signal processing algorithms can handle asymmetrical response signals, whose sampling points are varied with respect to their axial position. For this purpose, response signals for a tilted plane mirror are simulated with a lateral sampling interval of $\Delta x = 160\,\mathrm{nm}$. A tilted mirror is an example of practical relevance, since real measurement objects often show tilted specularly reflecting surface sections. A tilt angle $\theta_{\mathrm{tilt}}$ with respect to the $x$-axis leads to an axial shift of

$$\epsilon_z = \Delta z \mod \left( \frac{\Delta x \tan(\theta_{\mathrm{tilt}})}{\Delta z} \right) \tag{9}$$

between the sampling points of consecutive response signals. The function mod() represents the mathematical modulo operation. To avoid effects caused by surface roughness and measurement noise, the depth response signals are simulated for a perfectly flat mirror with a tilt angle of $\theta_{\mathrm{tilt}} = 15^\circ$ and an axial sampling interval of $\Delta z = 50\,\mathrm{nm}$.

Since real measurement results are usually affected by aberrations leading to asymmetric depth response signals, Seidel aberrations leading to a pupil function of the form

$$P(\theta_{\mathrm{in}}) = \mathrm{e}^{A \sin(\theta_{\mathrm{in}})} \mathrm{e}^{-\mathrm{i}B \sin(\theta_{\mathrm{in}})} \tag{10}$$

are considered in the simulations similarly to Corle et al. (Corle and Kino, 1996). The total simulated intensity $I(x,z)$ is calculated by

$$I(x,z) \sim \left| \int_0^{2\pi} \mathrm{d}\varphi_{\mathrm{in}} \int_0^{\arcsin(\mathrm{NA})} \mathrm{d}\theta_{\mathrm{in}} \sin(\theta_{\mathrm{in}}) \cos(\theta_{\mathrm{in}}) \Theta(\theta_{\mathrm{in}}, \varphi_{\mathrm{in}}) P(\theta_{\mathrm{in}}) \mathrm{e}^{-\mathrm{i}(k_{\mathrm{s},z}(\theta_{\mathrm{in}},\varphi_{\mathrm{in}}) - k_{\mathrm{in},z}(\theta_{\mathrm{in}}))(z+h(x))} \right|^2, \tag{11}$$

where the scattered and incident wave vectors $\mathbf{k}_{\mathrm{s}}(\theta_{\mathrm{in}}, \varphi_{\mathrm{in}})$, $\mathbf{k}_{\mathrm{in}}(\theta_{\mathrm{in}}, \varphi_{\mathrm{in}})$ with corresponding $z$-components $k_{\mathrm{s},z}$, $k_{\mathrm{in},z}$ as well the filter function $\Theta(\theta_{\mathrm{in}}, \varphi_{\mathrm{in}})$ are computed as it is already described by Siebert et al. (Siebert et al., 2022). $\varphi_{\mathrm{in}}$ and $\theta_{\mathrm{in}}$ represent the angles of conical illumination. The $x$ dependency is considered in form of the height function $h(x) = -\tan(\theta_{\mathrm{tilt}})x$.

The residual errors $\epsilon$ of the tilted profiles determined by the different signal processing approaches are depicted in Fig. 8, where the corresponding $\epsilon$ is calculated by subtracting the tilt from the resulting profiles. The profiles obtained by centroid algorithms exhibit the highest deviations from a straight line, followed by PF and GF methods. For determining the height values a threshold factor of 0.5 is used. The results obtained by CF show the lowest deviation. This result is qualified by the standard deviation $\sigma$ of each profile, as shown in Tab. 4. In comparison to PF and GF the standard deviation for CF is lower due to the asymmetrical course of the response signal, whereas a lower standard deviation can be expected for PF and GF compared to CF for a symmetrical signal course. However, asymmetrical courses are expected for response signals in practice.

| $\sigma_{\mathrm{LC}}$ (nm) | $\sigma_{\mathrm{SC}}$ (nm) | $\sigma_{\mathrm{PF}}$ (nm) | $\sigma_{\mathrm{GF}}$ (nm) | $\sigma_{\mathrm{CF}}$ (nm) |
|---|---|---|---|---|
| 4.96 | 3.06 | 1.32 | 1.31 | 0.28 |

**TABLE 4** Standard deviations $\sigma$ determined for the residual errors depicted in Fig. 8.

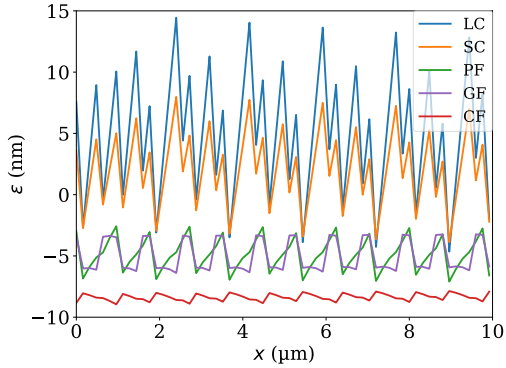


**FIGURE 8** Residual errors of profiles corresponding to a tilted plane mirror, depending on the signal processing algorithm.

## 2.3 | Repeatability

In the previous paragraph noise-free depth response signals are used to compare systematic deviations of different signal processing algorithms. In this section, the repeatability of these algorithms depending on the signal-to-noise ratio (SNR)

$$\mathrm{SNR} = 10 \log \left( \frac{\sigma^2_{\mathrm{signal}}}{\sigma^2_{\mathrm{noise}}} \right) \mathrm{dB}, \tag{12}$$

as specified by (Tereschenko, 2018) is investigated. Here, $\sigma^2_{\mathrm{signal}}$ and $\sigma^2_{\mathrm{noise}}$ represent the variance of the signal under investigation and the variance of the noise, respectively. Note that the noise amplitudes added to the asymmetrical response signals obey the normal distribution. Since only positive signal values are obtained from the camera used in a confocal microscope, the absolute values of the signals are taken for signal processing. Signals of different SNR are exemplarily depicted in Fig. 9 to illustrate the influence of the noise contribution. In order to analyze the repeatability of the signal processing algorithms 1000 signals, which are characterized by additive white noise contributions of given SNR, are simulated. Before calculating the height values by the signal processing algorithms, the intensity signals are low-pass filtered by multiplication with a Gaussian filter function in the Fourier domain. Finally, the empirical standard deviation $\sigma$ of the 1000 corresponding height values is calculated for each evaluation algorithm. In addition, the average $\bar{h}$ of the height values is determined. This procedure is repeated for signals of SNR values between 0 dB and 50 dB.

The empirical standard deviations obtained for thresholds of 0.6 and 0.8 are depicted in Fig. 10a and b, whereas the averaged height values are shown in Fig. 10c and d. Typical SNR values observed in practice are below 30 dB. In the case of the fitting approaches the determined standard deviations show an almost linear SNR dependence, where the standard deviations calculated by the CF approach are slightly higher compared to those obtained by the PF and the GF approaches. This is probably a consequence of the higher order used in the polynomial function of the CF method. Note that the standard deviations determined by PF and GF approaches are similar and thus can be hardly separated in Fig. 10. In the case of the centroid approaches, the standard deviations show a non-linear course in the range of approx. 10 dB and 30 dB. This is a result of a varying number of sampling points used for signal

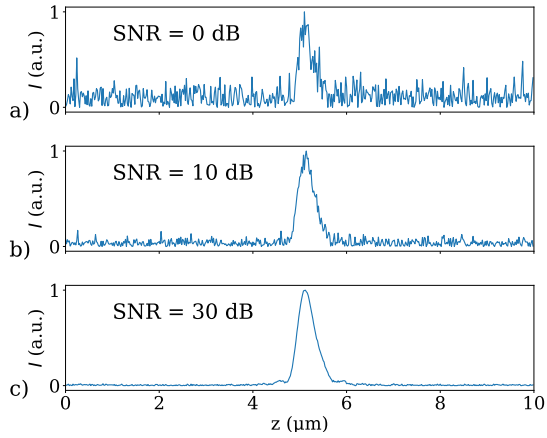


**FIGURE 9** Simulated depth response signals with different SNR values.

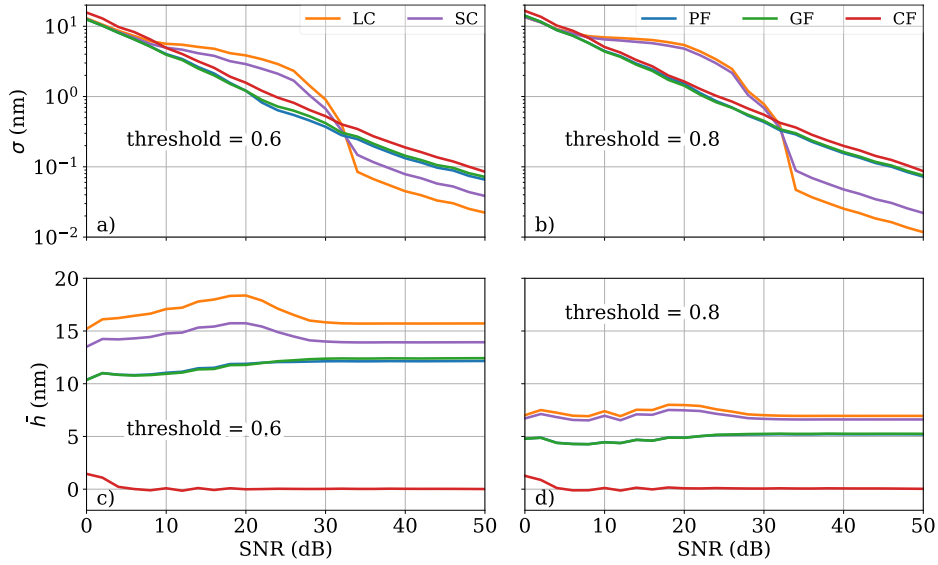


**FIGURE 10** Standard deviation $\sigma$ of 1000 repeated height values obtained by different signal processing algorithms depending on the SNR of the simulated asymmetric response signals for threshold values of 0.6 (a) and 0.8 (b) as well as corresponding averaged height values $\bar{h}$ in (c) and (d). Note that all averaged height values are related to $\bar{h}$ determined by the CF approach for a threshold of 0.6.

evaluation (similar to the previous section), as a consequence of the noise. Hence, the standard deviations obtained by the centroid methods are higher in the range of approx. 10 dB and 30 dB compared to those of the fitting approaches.

As discussed in Sec. 2.1, the height values determined by the CF approach are hardly affected by the used thresh-

old, whereas the values calculated by the other signal processing approaches show a dependency on the chosen threshold. This effect can also be observed by comparing the averaged height values $\bar{h}$ depicted in Fig.10c and d. While the LC, SC, PF and GF approaches provide values between approx. 12 nm and 16 nm for a threshold of 0.6, the values decrease to a range between 5 nm and 7 nm for a threshold of 0.8 and thus become closer to the height values obtained by the CF approach. Furthermore, the average $\bar{h}(\mathrm{SNR})$ determined by the CF method shows an almost constant course for both thresholds. $\bar{h}(\mathrm{SNR})$ increases only for low SNR values (<5 dB). In contrast, the averaged height values determined by the other depth discrimination algorithms show a non-constant course below 30 dB with variations up to 3 nm. Here, the values of the centroid methods exhibit the strongest variation. In order to analyze how well the intensity signal under investigation is represented by the approximated signal courses obtained by the fitting approaches, the standard deviation between the real intensity signal and the approximated signal course is calculated for each of the 1000 repeated intensity signals at identical SNR and finally, their average is taken. This procedure is repeated for each SNR value and compared in Fig.11. For Both thresholds, the averaged standard deviations determined by the PF and GF approaches exhibit higher values compared to the CF approach, as expected from the results listed in Tab. 1.

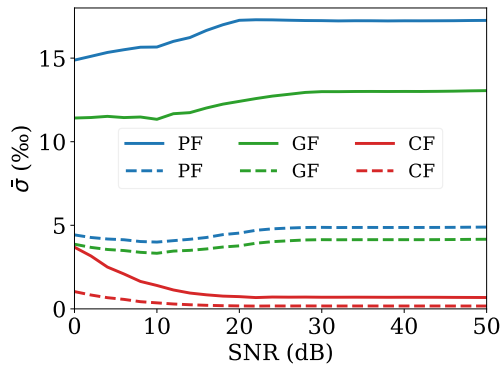


**FIGURE 11** Averaged standard deviations of the fitted curves obtained by the different signal processing algorithms with respect to the simulated intensity signal. The solid lines represent $\bar{\sigma}$ obtained for a threshold of 0.6 and 0.8 in case of the dashed lines.

## 2.4 | Layer thickness

Another example of improved accuracy achieved by the CF approach is related to layer thickness measurement. In the case of response signals obtained from a perfectly adjusted surface flat, it can be expected that the signal processing algorithms provide nearly the same relative height values independent of the lateral position even for asymmetric response signals. In contrast, response signals obtained from multiple layers show multiple peaks, which differ in their shape. This may result in offsets between the height values obtained for different layers at the same lateral position, especially if the signal processing algorithm cannot handle asymmetrical depth response signals.

For demonstration, a response signal obtained from a layer thickness standard is depicted in Fig. 12. This standard comprises a 4.1 µm thick SU-8 (transparent photoresist) located on a 10 nm thick chromium (Cr) layer, which is

deposited on an approx. 525 µm thick silicon layer (Brand et al., 2011). The right peak of the response signal results from the transition of air to SU-8 and exhibits a nearly symmetrical shape, whereas the left confocal peak results from the SU-8 to Cr transition and shows an asymmetrical course. While the signal processing algorithms represent the course of the right lobe well in almost the same manner, the course of the left lobe is well approximated only by the CF algorithm. Note that a threshold factor of 0.6 is used for signal processing. An increased threshold factor leads to a slightly improved representation of the signal course, as shown in (Hagemeier, 2022).

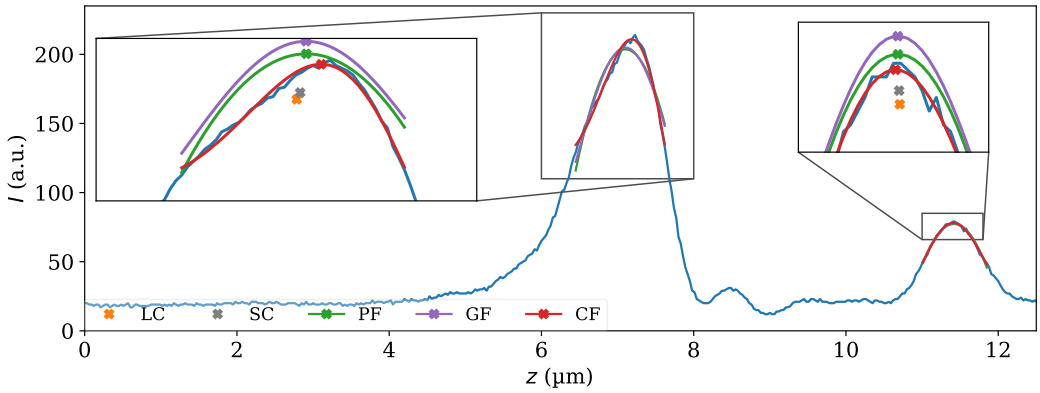


**FIGURE 12** Response signals (blue) obtained experimentally from a layer thickness standard, including the fits of the different fitting algorithms as well as crosses to mark the position determined by centroid approaches. Note that the curves shown in the magnified sections, which are determined by PF and GF as well as the crosses representing the LC and SC approaches, are shifted vertically by a certain offset to improve visibility.

Depending on the depth discrimination algorithm, multiple measured signal courses lead to varying height values for the left confocal peak, whereas those obtained for the right peak are similar, as represented by the lower and upper lines in Fig. 13 for a measured profile of the layer thickness standard. Assuming that the axial location of the corresponding signal maximum represents the correct height value, it can be concluded that the CF approach causes less deviations of the layer thickness values compared to the other algorithms. Averaged layer thicknesses $\Delta\bar{h}$ obtained by the different depth discrimination algorithms are listed in Tab. 5. Between the layer thickness determined by the CF and the other fitting approaches (PF and GF) is a difference of approx. 85 nm. The centroid algorithms lead to the highest deviations as shown by the averaged layer thicknesses of 140 nm and 120 nm between the CF and LC as well as SC methods. According to these results, the CF approach is the most suitable signal processing algorithm for calculating layer thicknesses. The determined standard deviations $\sigma_{\Delta\bar{h}}$ results from a lateral systematic deviation with respect to the nominal value and exhibit various values for the different algorithms.

| | LC | SC | PF | GF | CF |
|---|---|---|---|---|---|
| $\Delta\bar{h}$ (µm) | 4.35 | 4.33 | 4.30 | 4.30 | 4.21 |
| $\sigma_{\Delta\bar{h}}$ (nm) | 19.2 | 17.2 | 14.3 | 14.9 | 12.5 |

**TABLE 5** Averaged height differences $\Delta\bar{h}$ and standard deviations $\sigma_{\Delta\bar{h}}$ of the different layer thickness profiles depicted in Fig. 13.

Note that the refractive index is not considered for calculating the layer thickness, since it is not relevant for the above argumentation. In order to describe the difference between the measured height difference of 4.21 µm and the nominal height of 4.1 µm, the dependency of the refractive index and the NA must be considered. The layer thickness can be approximated by dividing the measured thickness by the refractive index of SU-8 for paraxial light rays. In case of increased NA the mathematical conversion of the measured to the real thickness becomes more complicated. Various approaches exist for this calculation as investigated in several studies (Sheppard et al., 1994; Cox and Sheppard, 2001; Brand et al., 2011; Kühnhold et al., 2015).

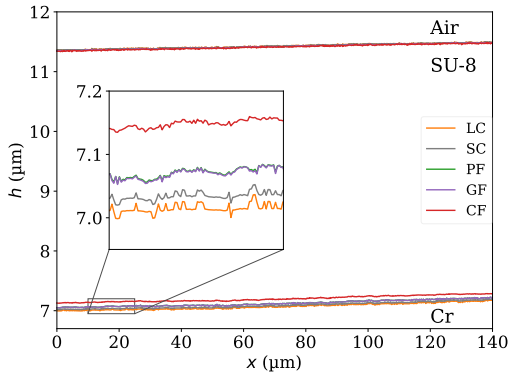


**FIGURE 13** Profiles of the measured height values obtained from a layer thickness standard using different signal processing algorithms.

## 3 | CONCLUSION

Depth response signals obtained by a confocal microscope exhibit more or less asymmetrical shapes. We have shown that the signal processing algorithm based on an exponential fitting function with a cubic argument is capable of treating asymmetrical confocal depth response signals. While the cubic algorithm determines the correct location of the intensity maximum, the positions calculated by other algorithms differ from the correct one. In the case of asymmetrical signals, the determined values of the other algorithms approx. matches the correct location if a high threshold is chosen and the intensity signal is symmetrically sampled around the location of the intensity maximum, what is hard to achieve in practice. Furthermore, we show that the cubic algorithm provides nearly the same values for varying threshold factors in case of asymmetrical and symmetrical signals, whereas the results of the other algorithms show significant variations. With respect to the repeatability determined for signals with various SNR, the cubic algorithm exhibits slightly higher values for the standard deviation compared to the other fitting approaches. However, if the number of the points sampling the confocal peak to be evaluated varies, the standard deviation increases for the other signal processing approaches and especially for the centroid approach. This effect is demonstrated for measurements obtained from tilted surfaces, where the axial positions of sample points vary between consecutive depth response signals. Likewise, the height values determined by the CF approach show the lowest deviation from the correct ones. Besides surface profilometry, layer thickness measurements are an important field of application where axially scanning confocal measurements are used. Layer thickness measurements are a further example for the

more reliable signal analysis of the CF approach. Hence, the cubic signal processing algorithm exhibits a robust and precise technique for height discrimination of asymmetrical confocal signals.

A disadvantage of the cubic algorithm is the higher computation time compared to the other algorithms presented in this work. However, due to increasing computational resources, the processing time is in an acceptable range, e.g. 984×984 depth response signals of 6 µm length and a step size of 30 nm are computed in 4050 ms for the cubic, in 3588 ms for the Gaussian and in 2915 ms for the parabolic fitting approaches as well as in 1932 ms for the square and in 1799 ms for the linear centroid methods using a personal computer with an Intel i9-9900K CPU (Intel Corporation). Furthermore, the computation time can be reduced by software optimization.

The field of application of the cubic algorithm is not limited to depth response signals obtained by confocal microscopes. Asymmetrical signals or spectra to be evaluated also occur if other sensor principles such as coherence scanning interferometry (Lehmann and Xie, 2015; Serbes et al., 2021), optical coherence tomography (Fercher et al., 2002, 2003), chromatic confocal microscopy (Chen et al., 2019; Claus and Nizami, 2020) and focus variation microscopy (Cui et al., 2018; Xu et al., 2022) are being used. The cubic signal processing algorithm can be applied to increase the accuracy of the detection of the maximum position of a signal or spectrum compared to common approaches based on symmetrical approximations.

## Conflict of interest

The authors declare no conflict of interest.

## References

Uwe Brand, Erik Beckert, Andreas Beutler, Gaoliang Dai, Christian Stelzer, Andreas Hertwig, Petr Klapetek, Jürgen Koglin, Richard Thelen, and Rainer Tutsch. Comparison of optical and tactile layer thickness measurements of polymers and metals on silicon or sio2. *Measurement Science and Technology*, 22(9):094021, 2011.

Cheng Chen, Jian Wang, Richard Leach, Wenlong Lu, Xiaojun Liu, and Xiangqian Jane Jiang. Corrected parabolic fitting for height extraction in confocal microscopy. *Optics Express*, 27(3):3682–3697, 2019.

Daniel Claus and Moaaz Rauf Nizami. Influence of aberrations and roughness on the chromatic confocal signal based on experiments and wave-optical modeling. *Surface Topography: Metrology and Properties*, 8(2):025031, 2020.

Timothy R Corle and Gordon S Kino. *Confocal scanning optical microscopy and related imaging systems*. Academic Press, 1996.

Guy Cox and Colin JR Sheppard. Measurement of thin coatings in the confocal microscope. *Micron*, 32(7):701–705, 2001.

Haihua Cui, Hao Wei, Xiaosheng Cheng, Xinguang Bian, and Ning Dai. An accurate simulation algorithm for focus variation microscopy. *SPIE Proceedings*, 10827:108270A, 2018.

Adolf F Fercher, Christoph K Hitzenberger, Markus Sticker, Robert Zawadzki, Boris Karamata, and Theo Lasser. Dispersion compensation for optical coherence tomography depth-scan signals by a numerical technique. *Optics Communications*, 204(1-6):67–74, 2002.

Adolf F Fercher, Wolfgang Drexler, Christoph K Hitzenberger, and Theo Lasser. Optical coherence tomography-principles and applications. *Reports on progress in physics*, 66(2):239–303, 2003.

Sebastian Hagemeier. *Comparison and investigation of various topography sensors using a multisensor measuring system*. PhD thesis, University of Kassel, Germany, 2022.

Sebastian Hagemeier, Markus Schake, and Peter Lehmann. Sensor characterization by comparative measurements using a multi-sensor measuring system. *Journal of Sensors and Sensor Systems*, 8(1):111–121, 2019.

Intel Corporation. *Intel Core i9-9900K Prozessor*. https://www.intel.de/content/www/de/de/products/sku/186605/intel-core-i99900k-processor-16m-cache-up-to-5-00-ghz/specifications.html, requested in 2023.

Taehoon Kim, Taejoong Kim, SeungWoo Lee, Dae-Gab Gweon, and Jungwoo Seo. Optimum conditions for high-quality 3D reconstruction in confocal scanning microscopy. *SPIE Proceedings*, 6090:60900W, 2006.

Peter Kühnhold, A Nolvi, Stanislav Tereschenko, I Kassamakov, E Hæggström, and P Lehmann. Transparent layer thickness measurement using low-coherence interference microscopy. *SPIE Proceedings*, 9525:555–565, 2015.

Peter Lehmann and Weichang Xie. Signal formation in depth-scanning 3D interference microscopy at high numerical apertures. *SPIE Proceedings*, 9660:216–227, 2015.

Chenguang Liu, Yan Liu, Tingting Zheng, Jiubin Tan, and Jian Liu. Monte Carlo based analysis of confocal peak extraction uncertainty. *Measurement Science and Technology*, 28(10):105016, 2017.

Tobias Pahl, Sebastian Hagemeier, Jörg Bischoff, Eberhard Manske, and Peter Lehmann. Rigorous 3D modeling of confocal microscopy on 2D surface topographies. *Measurement Science and Technology*, 32(9):094010, 2021.

Maik Rahlves, Bernhard Roth, and Eduard Reithmeier. Systematic errors on curved microstructures caused by aberrations in confocal surface metrology. *Optics Express*, 23(8):9640–9648, 2015.

Maik Rahlves, Bernhard Roth, and Eduard Reithmeier. Confocal signal evaluation algorithms for surface metrology: uncertainty and numerical efficiency. *Applied Optics*, 56(21):5920–5926, 2017.

AK Ruprecht, TF Wiesendanger, and HJ Tiziani. Signal evaluation for high-speed confocal measurements. *Applied Optics*, 41 (35):7410–7415, 2002.

Jörg Seewig, Indek Raid, Christian Wiehr, and Bini Alapurath George. Robust evaluation of intensity curves measured by confocal microscopies. *SPIE Proceedings*, 8788:87880T, 2013.

Hüseyin Serbes, Pascal Gollor, Sebastian Hagemeier, and Peter Lehmann. Mirau-based CSI with oscillating reference mirror for vibration compensation in in-process applications. *Applied Sciences*, 11(20):9642, 2021.

Rongjun Shao, Weiqian Zhao, Lirong Qiu, Yun Wang, and Ruirui Zhang. Accuracy evaluations of axial localisation algorithms in confocal microscopy. *SPIE Proceedings*, 10819:108191O, 2018.

Colin JR Sheppard, T John Connolly, Jin Lee, and Carol J Cogswell. Confocal imaging of a stratified medium. *Applied Optics*, 33(4):631–640, 1994.

Markus Siebert, Sebastian Hagemeier, Tobias Pahl, Hüseyin Serbes, and Peter Lehmann. Modeling of fiber-coupled confocal and interferometric confocal distance sensors. *Measurement Science and Technology*, 33(7):075104, 2022.

SiMETRICS GmbH. *Resolution Standard Type RS-N*, 2009. http://www.simetrics.de/pdf/RS-N.pdf, requested in 2023.

Jiubin Tan, Chenguang Liu, Jian Liu, and Hongting Wang. Sinc2 fitting for height extraction in confocal scanning. *Measurement Science and Technology*, 27(2):025006, 2015.

Stanislav Tereschenko. *Digitale Analyse periodischer und transienter Messsignale anhand von Beispielen aus der optischen Präzisionsmesstechnik*. PhD thesis, University of Kassel, Germany, 2018.

T Wilson and AR Carlini. The effect of aberrations on the axial response of confocal imaging systems. *Journal of Microscopy*, 154(3):243–256, 1989.

Weichang Xie. *Transfer characteristics of white light interferometers and confocal microscopes*. PhD thesis, University of Kassel, Germany, 2017.

Xin Xu, Sebastian Hagemeier, and Peter Lehmann. Outlier elimination in rough surface profilometry with focus variation microscopy. *Metrology*, 2(2):263–273, 2022.